

Identification of compounds adsorbed and deposited on the Ni-Mo catalysts surface of alumina and SBA-15 by DRIFTS, Raman and TPO Analyses before and after Guaiacol hydrodeoxygenation.

Rubens W.S. Lima

Universidade de São Paulo, Escola Politécnica, Departamento de Engenharia Química, Av. Prof. Luciano Gualberto, travessa 3, no. 380, 05508-010, São Paulo, Brasil

Thiago L.R. Hwer

Universidade de São Paulo, Escola Politécnica, Departamento de Engenharia Química, Av. Prof. Luciano Gualberto, travessa 3, no. 380, 05508-010, São Paulo, Brasil

Rita M.B. Alves

Universidade de São Paulo, Escola Politécnica, Departamento de Engenharia Química, Av. Prof. Luciano Gualberto, travessa 3, no. 380, 05508-010, São Paulo, Brasil

Martin Schmal (✉ schmal@peq.coppe.ufrj.br)

Universidade de São Paulo <https://orcid.org/0000-0001-6816-523X>

Research

Keywords: Guaiacol Adsorption, hydrodeoxygenation, Ni-Mo, SBA-15, Alumina, DRIFTS, Raman

Posted Date: March 29th, 2021

DOI: <https://doi.org/10.21203/rs.3.rs-321528/v1>

License:  This work is licensed under a Creative Commons Attribution 4.0 International License.

[Read Full License](#)

Abstract

We studied and identified compounds adsorbed or deposited on the catalysts surface of the Ni-Mo supported on alumina and SBA-15, before and after hydrodeoxygenation of a bio-oil model (guaiacol). Marked differences were observed on both catalysts through DRIFTS and Raman spectroscopy showing that the alumina-supported catalyst contains deposits of aromatic and oxygenated organic substances, while the carbon deposits on the SBA-15 as aliphatic simple molecules. TPO analyses confirm that the carbon deposited on the NiMo/SBA-15 catalyst were light polymer types, mainly nanotubes and nano fibers, while on the alumina catalyst the mainly carbon species formed were graphite type and heavier carbons. Post reaction analysis of the catalysts showed coke formation and carbon deposition rate of $1.14 \text{ mg}_{\text{coke}} \cdot \text{g}_{\text{cat}}^{-1} \text{ h}^{-1}$ for NiMo/SBA-15 and the deactivation was 44 % higher for the NiMo/ Al_2O_3 with $1.65 \text{ mg}_{\text{coke}} \cdot \text{g}_{\text{cat}}^{-1} \text{ h}^{-1}$ of carbon deposition rate.

1 Introduction

Biomass is an alternative to replace fossil energies, since it is a raw material of low costs and high versatility, which makes it ideal for use as a source of carbon to produce valuable renewable fuels and chemicals using modern pyrolysis techniques [1][2]. It is notable that biomass materials contain high oxygen compounds, and therefore, the deoxygenation through catalytic HDO reactions allows their transformation into hydrocarbon fuels.

However, the main challenge is to develop catalysts able to eliminate as much oxygen as possible without removing the carbon from the fuel and using a minimum amount of hydrogen[3–5]. The hydro deoxygenation (HDO) of bio-oils, lignin and the reaction catalyst stability with time-on-stream is crucial for the industrial utilization of biomass to produce fuels and chemicals

Nickel(Ni) and molybdenum (Mo) or cobalt (Co) and molybdenum sulfide(MoS_2) have been employed in HDO process with different supports, like SiO_2 , ZrO_2 , CeO_2 , TiO_2 , La_2O_3 oxides, as well as their composites [5]. Lastly, mesoporous silica, such as SBA-15, SBA-16 and MCM-41[6, 7]; zeolites MZ-5, HZSM-5, H-Beta and HY[8–10] and allotropic forms of carbon, for instance active carbon, carbon nanotubes and carbon nanofibers[11, 12] have been used.

The deposition compounds of HDO catalysts is also a key problem, mainly due to severe coke formation [13]. The carbon formation occurs via polymerization and poly-condensation reactions on the acid sites of the support, producing polyaromatic species that may block the active sites of the catalysts[14]. Acidity plays an important role in both selectivity and deactivation, since acid sites can favor specific reaction routes and, thus, generating undesired products, such as polymeric carbon (coke) and heavy organic products[15]. Echeandia et al.[16] proved that there is a proportional ratio between coke production and catalyst total acidity, using palladium supported on HY zeolites in continuous HDO of phenol. Sankaranarayanan et al.[7] studied Ni and Co catalysts on HZSM-5 zeolite, SBA-15 silica and Al-SBA-15 alumino-silicate supports and concluded that nickel, when associated with supports with

moderate acidity and high surface area, such as HZSM-5 and Al-SBA-15, have better results for oxygen elimination and hydrogenation of aromatic rings, which makes them ideal catalysts for HDO process. Recently, Hower et al. [17] studied nickel and molybdenum nanoparticles on silicon aluminum phosphate (SAPO-11) and mesoporous silica (SBA-15), respectively, and compared with γ -Al₂O₃ support. These catalysts exhibited excellent catalytic activity for hydrodeoxygenation (HDO) of anisole and the hydrodeoxygenation and hydro-dearomatization reactions are strongly affected by the support nature due to the Brønsted and Lewis acid sites[17].

However, there are different causes that provoke route directions of the hydrogenation process for the formation of HDO and HDA or deoxygenation to aliphatic compounds affecting of the catalyst, which is related to the adsorbed species or intermediate compounds at the surface of the catalysts, which are really the precursors for the selectivity that depend significantly on the supports, in particular, the surface acid sites and dispersions of metallic phases. These species are precursors of carbon formation.

Therefore, we study the nature of the compound deposition occurring on alumina and SBA-15 supports with Ni-Mo, and identification by the adsorption of intermediate compounds formation during the hydrogenation process of a model compound of bio-oils, analyzing the surface species deposited on the catalysts by comparing before and after reaction. For this purpose, we used spectroscopic analyses, in particular DRIFTS and Raman techniques, complemented by TGA and TPO analyzes.

2 Experimental

2.1 Catalysts preparation

The SBA-15 support was synthesized following the method described elsewhere [15][18]. In short, 4 g of the polymer Pluronic P213 (PEO20PPO70PEO20) from BASF was dissolved in 122 g of HCl 2M solution and kept under stirring for 1 h. Then, 8.6 g of tetra orthosilicate (Fluka) was added and the solution was continuously stirred for 24 h. The mixture underwent a hydrothermal treatment during 48 h at 100 °C in an autoclave, washed thoroughly with deionized water and dried at room temperature. Finally, the polymeric support was calcined at 540 °C in N₂ flow for 2h and in air for 4 h. The alumina support (γ -Al₂O₃) was acquired from Degussa and calcined at 500 °C for 20 h with synthetic air flow and at a rate of 5 °C/min. Then, nickel and molybdenum were added by wet impregnation in separate. For the required amount of Molybdenum oxide, the salt precursor ((NH₄)₆Mo₇O₂₄·4H₂O) was dissolved in deionized water and mixed with the support and the suspension was stirred for 2 h. Afterwards, the mixture was lyophilized for eliminating the residual solvent and calcined at 500 °C for 2 h in air flow of 50 ml min⁻¹. Then, the Ni(NO₃)₂·6 H₂O salt (ACROS Organics) was dissolved similarly and impregnated in sequence and calcined under similar conditions.

2.2 Characterizations

The textural properties of the catalysts were analyzed by N₂ adsorption isotherm, using the Quantacrome volumetric adsorption analyzer (model 100E). The surface area was determined by BET technique and the pore distribution obtained by the BJH method[19,20]. Complete characterization of these materials were reported elsewhere [17].

The metal surface areas and dispersions of the catalysts were determined by H₂ chemisorption in an ASAP 2020C chemisorption system (Micrometrics). In a typical analysis, a 120 mg of sample was loaded in the reactor and dried with a He flow for 1h at 300 °C and at rate of 10°C min⁻¹. Then, switched to 5% H₂/Ar flow and reduced for 4 h at 550 °C and 10 °C min⁻¹. After cooling down to 35 °C and evacuation the total and reversible isotherms and, consequently, the metallic surface areas and dispersions were obtained.

The total acidity of the supports and catalysts was measured by the temperature programmed desorption of NH₃ (NH₃-TPD). Approximately 200 mg of the sample was pretreated with a flow of He (30 ml min⁻¹) at 250 °C for 1 h and at 5 °C min⁻¹. After cooling to room temperature, the gas was replaced by a flow of 4% NH₃ / He (60 ml min⁻¹) at 150 °C for 1 h and cooled to room temperature under pure He flow. Then ammonia desorption took place, raising the temperature at 20 °C min⁻¹ up to 700 °C. The amount of desorbed ammonia was measured on a quadrupole mass spectrometer (Balzers, PRISMA)

The adsorption on the catalysts surface was studied by in-situ DRIFTS cell using a Nicolet Nexus 870 instrument with a DTGS-TEC detector and a Thermo Spectra-Tech reaction chamber with ZnSe windows. To reduce the sample, H₂ was flowed (40mL/min) at 500 °C for a period of 1 h and the temperature was decreased to 200 °C while He was flowed to record a spectrum for use as a background. Guaiacol adsorption involved bubbling He (40 mL/min) through a saturator with guaiacol/n-heptane solution (2% guaiacol, mass %) for 30 min, followed by a He purge. Spectra were recorded at 200, 250 and 300 °C. The scan resolution was 4 cm⁻¹ and 512 scans were taken.

The Fourier-transform infrared spectroscopy (FTIR) measurements were performed in a Shimadzu IRPrestige-21 spectrometer using 20 mg of the sample pelletized with KBr. Spectra before and after reaction were recorded in a wavelength between 400-4000 cm⁻¹.

The Raman spectrometer, a Renishaw Confocal Raman Microscope model with excitation wavelength of 632 nm, was used for determining carbon deposition after reaction. The crystallite sizes L_a of the graphite deposited over the catalysts surface were obtained, according to the Equation 1[21]:

$$L_a(nm) = 2,4 \cdot 10^{-10} \lambda_{laser}^4 \left(\frac{I_D}{I_G} \right)^{-1} \quad (1)$$

Where, λ_{laser} is the laser wave length used in the Raman experiments, I_D and I_G are the intensity Raman D and G bands of the carbon depositions.

Thermogravimetric analysis (TGA) and differential thermal analysis (DTA) were performed under a synthetic air flow (100 mL min⁻¹), using a Shimadzu DTG-60 equipment. The samples were heated from room temperature up to 900 °C at 10 °C min⁻¹.

The carbon deposits formed on the catalysts surface were analyzed by temperature programmed oxidation technique (TPO) in an ASAP 2020C chemisorption system (Micromeritics). In a typical analysis, 120 mg of the sample was dried with He, at 90 mL min⁻¹ flow and 300 °C for 30 minutes. Then, switched to the O₂/Ar mixture (5 Vol. % O₂) flow at 60 mL min⁻¹ and heated up to 600 °C at 10 °C min⁻¹.

2.3 Catalytic activity tests

The catalytic tests were carried out in a fixed bed flow reactor system at 15 kgf.cm⁻² pressure. The mass around 200 mg was pre-treated in situ with pure H₂ (AGA) at 50 mL min⁻¹ flow, at 500 °C for 4 h, and then cooled to the reaction temperature (200, 250 or 300 °C) under hydrogen atmosphere. The feed mixture consisted of 2 % w/w Guaiacol (MERCK) in heptane P.A. (Aldrich) pumped at 14.8 mL min⁻¹, and carried with H₂ flow at 100 mL min⁻¹. The reactor input (reactants) and output (products) compounds were maintained in vapor phase, with a steel line heated at 125 °C, until the 6-way valve of the gas chromatograph. The organic compounds were analyzed by gas chromatography in a Shimadzu CG17A equipment, with FID and mass spectrometric detectors, capillary column CP sil 5CB and automatic injection. Conversion, selectivity and reaction rates were determined according to equations 2-4, respectively.

$$X(\%) = \frac{(Reactant)_{in} - (Reactant)_{out}}{(Reactant)_{in}} \cdot 100 \quad (2)$$

$$S_i(\%) = \frac{C_i}{\sum C_i} = \frac{Product_{if_i} / \sum Product_{if_i}}{\sum (Product_{if_i} / \sum Product_{if_i})} \cdot 100 \quad (3)$$

$$r_{cat} = F_0 \cdot \frac{X}{100} \cdot \frac{M_{GUA}}{m_{cat}} \quad (4)$$

Where, F_0 is the molar flow rate of Guaiacol, M_{GUA} is the Guaiacol molecular weight and m_{cat} , the mass of the catalyst.

3 Results And Discussion

Table 1 presents the surface areas of the supports Al_2O_3 and SBA-15, $279 \text{ m}^2 \text{ g}^{-1}$ and $630 \text{ m}^2 \text{ g}^{-1}$, respectively. The SBA-15 presents a total pore volume of $1.17 \text{ cm}^3 \text{ g}^{-1}$ and an average pore diameter of 7 nm. The surface area and the pore volume of the catalyst NiMo/SBA-15 decreased to $332 \text{ m}^2 \text{ g}^{-1}$ and $0.68 \text{ cm}^3 \text{ g}^{-1}$, respectively. The surface area of NiMo Al_2O_3 catalyst also decreased, as shown in Table 1.

Table 1
Textural properties of the supports and Ni-Mo catalysts.

Catalyst	Specific surface area ($\text{m}^2 \text{ g}^{-1}$)	Pore Volume ($\text{cm}^3 \text{ g}^{-1}$)	Pore diameter (nm)	Metal Acidity Dispersion NH_3 -TPD (%) ($\mu\text{mol g}^{-1}$)
SBA-15	630	1.17	7	
Al_2O_3	279	0.95	7.8	731
NiMo/SBA-15 fresh	332	0.68	7.4	1.8 470
NiMo/SBA-15 spent	261	0.59	6.5	
NiMo/ Al_2O_3 fresh	233	0.78	7.9	0.4 54
NiMo/ Al_2O_3 spent	157	0.64	9.7	

The total acidity of the supports and catalysts was measured by Temperature Programmed Desorption of NH_3 (NH_3 -TPD). Table 1 showed that SBA15 has a total acidity of $470 \mu\text{mol g}^{-1}$, while the alumina of $548 \mu\text{mol g}^{-1}$. The excess of acidity ($> 890 \mu\text{mol g}^{-1}$) causes an increase of polymerization products, resulting in the formation of coke at the catalyst surface [22].

IR spectra of Guaiacol adsorption

The IR spectra of Guaiacol adsorbed on NiMo-SBA15 and NiMo- Al_2O_3 are compared in Fig. 1. In the high frequency region, bands at 2966 , 2935 and 2873 cm^{-1} , corresponding to $\nu(\text{CH}_{\text{ring}})$ and $\nu(\text{CH}_3)$ of guaiacol, Guaiacol, are present in the spectra of both samples, Fig. 1B. Alike for NiMo- Al_2O_3 , no band of free OH groups of guaiacol at 3555 cm^{-1} was detected in the NiMo-SBA15 spectrum. The guaiacol adsorption spectra on NiMo- Al_2O_3 , in low frequency region, exhibits characteristic bands of aromatic ring vibration [$\nu(\text{CC}_{\text{ring}})$] at 1581 cm^{-1} and broad band centered at 1463 cm^{-1} related to $\delta(\text{CH}_3)$ vibration and

with $\delta(\text{OH})$ contribution. The poor resolved band at 1355 cm^{-1} , corresponding to $\delta(\text{OH})$ vibration, close to that observed for free gGuaiacol, Guaiacol, is present in its spectra [23]. For the NiMo-SBA15, the guaiacol adsorption spectrum at low frequencies was very different from that observed for NiMo- Al_2O_3 . The band characteristic of the $\nu(\text{CC}_{\text{ring}})$ vibration shifts to 1599 cm^{-1} and the band at 1492 cm^{-1} of the $\nu(\text{CC}_{\text{ring}})$ is clearly observed. The bands of $\delta(\text{CH}_3)$ vibration, a triplet between $1463 - 1442\text{ cm}^{-1}$, are present in the NiMo-SBA15 spectra. The band at 1355 of $\delta(\text{OH})$ vibration does not appear in the NiMo-SBA15 spectra, which indicates the absence of free phenol on its surface.

After guaiacol adsorption, the chamber was cleaned with He flow during 30 minutes and temperature increased up to 300°C , Fig. 2A. In the high frequency region, guaiacol was still adsorbed on the SiO_2 surface and it is possible to observe the low intensity bands in the range $3000 - 2800\text{ cm}^{-1}$. In fact, the guaiacol adsorption leads to a decrease of free Si-OH groups, as evidenced in the negative band at 3750 cm^{-1} , and this behavior indicates the silanol groups were perturbed by the interaction with guaiacol through its aromatic ring[24, 25].

For the NiMo-SBA15 after evacuation and with increasing temperature from 200 to 300°C , the bands at 1587 and 1492 cm^{-1} , corresponding to aromatic ring vibrations $\nu(\text{CC})$ were still present, however, the band 1454 cm^{-1} is more sensitive and disappeared at 300°C . The broad multicomponent envelope at 1353 to 1267 cm^{-1} is characteristic of the stretching modes of C-OH and C-OCH₃. The IR spectra obtained for Guaiacol interaction on the NiMo- Al_2O_3 surface are show in Fig. 2B. At 200°C , the intensity of the 1463 cm^{-1} band decreases and the bands at 1581 cm^{-1} and 1359 cm^{-1} are still the same. However, with increasing temperature to 250 and 300°C , the bands attributed to the vibrational modes $\nu(\text{C} = \text{C}_{\text{ring}})$ 1581 and 1355 cm^{-1} of $\delta(\text{OH})$ decreased. The opposite was observed for the new band at 1496 cm^{-1} , and the band at 1454 cm^{-1} , assigned to $\nu(\text{C} = \text{C}_{\text{ring}})$ and CH_3 vibrational modes, respectively. In the same way, but less intense, new bands can be observed in the $1200 - 1300\text{ cm}^{-1}$ region, which are attributed to the $\nu(\text{CO})$ vibration.

hydrodeoxygenation of Guaiacol

The catalytic test results of conversion and reaction rates at 200 , 250 , 300°C are shown in Table 2 and Fig. 3.

Table 2
Reaction conditions, conversions, product distribution and HDO and HDA conversions

Catalyst	NiMo/SBA-15			NiMo/Al ₂ O ₃		
	200	250	300	200	250	300
Space velocity WSHV (h ⁻¹)	1.57			1.24		
Temperature (°C)	200	250	300	200	250	300
Conversion (%)	3.7	74.5	84.7	5.1	45.0	72.6
HDO (%)	92.1	74.3	66.5	37.9	31.5	30.8
HDA (%)	84.2	48.7	35.3	23.1	12.3	2.7
Selectivity (%)						
Benzene	16.7	8.6	1.3	3.3	1.1	0.3
Cyclohexane	29.1	13.9	11.0	6.8	3.3	0.4
Cyclohexene	38.5	26.2	19.5	12.9	7.9	1.9
Phenol	10.5	17.4	34.2	16.3	24.8	41.3
o-Cresol	0.0	18.4	8.0	7.7	8.5	11.3
Monooxygenates	5.3	15.5	20.2	5.8	4.9	3.8
Dioxygenates	0.0	0.0	2.3	47.2	49.4	41.0

The conversion of guaiacol increased with temperature. At 300°C, the conversions were 85 % for NiMo on SBA-15 and 73 % for alumina catalysts, respectively. These results are in good agreement with the literature for HDO reactions [27, 28–31]. Figure 3B displays the reaction rate with increasing temperature and both catalysts. Note that the influence of the support was significant, indicating that the NiMo/SBA-15 was higher than NiMo/Al₂O₃.

Selectivity and products distribution

The selectivity and products are presented in Table 2 and Fig. 4 and show significant influence of the support. In fact, comparing both catalysts, three main aspects may be analyzed: the selectivity of non-oxygenated compounds is higher on NiMo/SBA-15 than on NiMo/Al₂O₃ for all temperatures; the selectivity to phenol is higher on NiMo/Al₂O₃ for all temperatures; and the deoxygenated compounds (catechol, methyl Guaiacol and derivatives) are formed mostly on NiMo/Al₂O₃ for all temperatures. The selectivity to phenol is higher on NiMo/Al₂O₃ for all temperatures. SBA-15 support presents basically Si-OH groups, which act as Lewis acid sites. The SBA-15 has higher ability for direct demethoxylation of Guaiacol resulting in phenol, while the alumina support has had more ability for demethylation, forming catechol, which is transformed to phenol through hydrogenolysis [5, 29–32].

It depends on presence of the metallic oxide sites Ni and Mo on the surface. The first for activation of hydrogen and the second for adsorption of oxygenated compounds, due to the oxo facility [33]. Therefore, the molybdenum on the surface of SBA-15 favored the demethyloxylation of the guaiacol molecule, forming phenol.

In fact, the alumina support presents greater amount and higher acid forces than the SBA-15, thus directing the reaction to a different route. The strong Lewis sites adsorb guaiacol molecules through the oxygen of the methoxyl groups, and consequently, favors the rupture of methyl and adsorption on the surface [34, 35]. Therefore, the main product is catechol and its methyl derivatives.

In fact, phenol can also be formed through hydrogenolysis of catechol due to the Mo sites on the surface of the supports, which explains the higher amount of the phenol formed on the alumina catalyst compared to the SBA-15 catalyst, in accordance to [30]. Indeed, the energy needed for total elimination of oxygen for both catalysts is different. On silica, it needs the rupture of the ether bindings $C(sp^2)-OCH_3$ (356 kJ/mol) and the phenolic bonding $C(sp^2)-OH$ (414 kJ/mol), while for the alumina catalyst, occurs the rupture of the methyl group $C(sp^3)-OC(sp^2)$ (247 kJ/mol), followed by two phenolic bonds. Therefore, the SBA-15 catalyst has greater facility to generate non-oxygenated compounds or with less oxygen atoms, following a reaction energetically more favorable than on the alumina catalyst. Results evidence that the selectivity depends on the support but significantly on the product distribution.

Analyses after reaction

IR analyses

Figure 5 shows the FTIR spectra of the fresh NiMo/SBA-15 and NiMo/Al₂O₃ catalysts, respectively. The NiMo/SBA-15 catalyst presented bands relative to Si-O-Si and Si-OH bonds of the silica support and bindings relative to Mo = O and Mo-O-Mo of the molybdenum oxide. The bands 800–812 cm⁻¹ are relative to the stretched symmetric Si-O-Si bridged structure of the mesoporous silica; the band at 950 cm⁻¹ refers to the stretched silanol band of Si-OH on the surface due to the defects of the structure; the band at 1090 cm⁻¹ corresponds to the asymmetric bridged Si-O-Si bonding; and finally the band 3440 cm⁻¹ to the silanol groups of Si-OH and hydroxyls of the water adsorbed on the catalyst surface [36, 37]. The band 1640 cm⁻¹ is attributed to the adsorbed water [45]. In this spectrum it was not possible to detect the Ni-O bond, which occurs between 400 and 500 cm⁻¹, as well as the bands relative to the bonding of Mo = O of the MoO₃, which would appear between 800 a 1000 cm⁻¹, probably because the silica bands overlap the nickel and molybdenum oxide band [38, 39]. The Mo-O-Mo bonding, that occurs in this range [40], shows similar behavior. Finally, the small band at 704 cm⁻¹ can be attributed to the stretching symmetric band of Ni-Mo-O present on the mixed oxide NiMoO₄ [41].

After reaction it is noteworthy to observe significant modification in the IR spectrum of the silica catalyst. New bands appeared at 1390 and 1470 cm⁻¹, which are assigned to the rotation vibration and folding of

C-H bonds of methyl groups [42]. The formation of $-CH_3$ groups at the catalysts surface during the reaction is closely related to the deactivation due to the carbon deposition on its surface [43]. The band intensity is low, in agreement with the literature, since on silica supports the carbonaceous species formation is low [44].

The infrared spectra of the $NiMo/Al_2O_3$ catalyst before and after reaction are shown in Fig. 5B. A broad band was observed between 600 and 1000 cm^{-1} , which can be assigned to the unfolding O-Al-O bonding and the stretching bond of Al-O [45–47]. As observed previously the Mo = O and Mo-O-Mo bands appear in the same interval and are less sensitive at 625 and $750\text{--}850\text{ cm}^{-1}$. The first band was not observed on the SBA-15 support, which evidenced the Mo-Al-O bond interacting with the alumina support, due to the presence of the $Al_2(MoO_4)_3$, as identified by XRD [48]. The bands between 750 and 850 cm^{-1} are assigned to the stretching of the Mo = O terminal bond (perpendicular to the MoO_3 laminar structure) and the stretching bond of Mo-O-Mo [49]. The band 1630 cm^{-1} evidenced the H-O-H bonding of water at 3450 cm^{-1} to the vibration of hydroxyls on the surface (Al-OH) and of water in the lattice.

After reaction the spectrum of the alumina supported catalyst (Fig. 5B) presented significant differences in the range 1000 and 1600 cm^{-1} , with appearance of new bands at 1014 , 1102 , 1260 e 1500 cm^{-1} . Indeed, the bands at 1014 cm^{-1} , 1102 cm^{-1} , 1260 cm^{-1} , and 1500 cm^{-1} are attributed to the unfolding C-H band bonded to the aromatic rings, the stretching C-O(alcohol/phenolic), stretching of C-O (ether) and stretching of aromatic C = C bands, respectively, according to Silverstein [42]. Note, that all these bands evidenced the aromatic compounds adsorbed on the surface of the alumina catalyst. Indeed, there are reports indicating that alumina support favors the formation of heavy aromatic compounds due to the strong adsorption of Guaiacol on its surface. This kind of molecules could favor the formation of methyl-substituted derivatives, like ($-CH_3$), hydroxyl ($-OH$) or other aromatic compounds on the catalysts surface in agreement with the literature [3, 34, 43, 50]. As consequence, these organic compounds promote coke deposition on the catalyst and blocking surface active sites. The $-CH_3$ band is lighter for the $NiMo/SBA-15$ catalyst, suggesting easier desorption, probably due to the substituted reactions with the heavier adsorbed products on SBA-15. In fact, aromatic bands were not observed on SBA-15, which adsorbed preferentially methyl groups, suggesting higher stability concerning the deactivation process when compared to the alumina support.

Raman spectroscopy analyses

The Raman spectroscopy of the catalysts was performed for identifying the structures of the synthesized materials between 300 to 1100 cm^{-1} , and the carbon structure formed on the catalysts surface after the hydro deoxygenation of the guaiacol in the wavelength range of $1100\text{--}1800\text{ cm}^{-1}$, Fig. 6. For $NiMo/SBA-15$ fresh catalysts, there are stretching bonds of Si-O-Si at 453 cm^{-1} and stretching of siloxane rings of SBA-15 support at 484 cm^{-1} .

The band at 389 cm^{-1} is assigned to the bending bonding of O-Mo-O of the MoO_3 and the band at 723 cm^{-1} is assigned to the symmetric stretching bonds of Ni-Mo-O of the NiMoO_4 . Asymmetric stretching bonds of O-Mo-O of the MoO_3 occurred at 829 and 900 cm^{-1} . Finally, the band located at 958 cm^{-1} is assigned to the stretching bonds of Mo = O on the NiMoO_4 and Mo-O on the polymeric MoO_x species. The presence of these bindings confirms the presence of MoO_3 e NiMoO_4 species, as observed and identified by XRD results. Moreover, the identified band at 958 cm^{-1} is attributed to the NiMoO_4 species, which indicates that this oxide is a well-defined crystalline structure, in agreement with the literature[51–53].

The Raman spectrum of the NiMo/SBA-15 after reaction between 1000 and 1800 cm^{-1} indicates the broad carbonaceous species present on the catalyst surface, from graphite to amorphous carbons. In fact, the band at 1324 cm^{-1} is assigned as D1 carbon structures that correspond to unordered and poorly organized carbon [54]. On the other hand, at 1589 cm^{-1} is the G band, indicating the well-organized structure like graphite, carbon nanotubes or carbon fibers, according to SHANMUGAN et al.[55]. Besides, the band at 1265 cm^{-1} shows the D4 band and the bands 1485 cm^{-1} and 1552 cm^{-1} , identified as D3 are assigned to disordered graphite matrices and amorphous carbons, respectively [54, 56]. It seems that on the silica support the carbon structure is less organized (D1 band) and exhibits defects (D4 band), and therefore, less organized structures like graphite (G band). These results corroborate with the TPO analyses, which demonstrated the deposition of light carbons deposited on NiMo/SBA-15. It can also be attributed to defects of polymeric structures, like carbon nanotubes or fibers. The organization degree of the carbon structure formed at catalysts surface was measured from the ratio between D and G band intensities. For NiMo/SBA-15, this ratio is 2.05 suggesting higher disordered carbon structure formed on the catalysts surface during the HDO reaction. The crystallite size L_a of the carbon deposits was calculated according to Eq. 1. For NiMo/SBA-15 spent catalysts it was 18.8 nm, Table 3. This value is greater than the mean pore sizes of the SBA-15 support, around 8.77nm, as observed by TEM analyses [17], which suggests that most carbon was deposited on the surface and blocked most of the pores of the support. In fact, it decreased the surface area of the NiMo/SBA-15 after reaction, and provoked high deactivation due to the carbon deposition.

The Raman results of the fresh NiMo/ Al_2O_3 catalyst present similar vibration bands as observed for SBA-15 and MoO_3 was the predominant phase, while the NiMoO_4 appeared with lower intensity, not observed through XRD. The well-defined band of the polymeric MoO_3 indicates higher degree of crystallization of the molybdenum oxide phase, which corroborates with the great crystallite sizes calculated from the X-ray diffraction pattern.

From the Raman spectrum of the NiMo/ Al_2O_3 after reaction, it is possible to observe the bands at 1271 cm^{-1} (D4), 1343 cm^{-1} (D1), 1462 cm^{-1} (D3) and 1593 cm^{-1} (G) assigned to the different carbon allotropes. The spectrum shows well defined D1 and G bands, and shoulders, as indicated in bands D4 and D3. The calculated ratio between I_D/I_G was 0.99, indicating that the carbon formed deposits with similar proportion of graphitic allotrope and disordered carbon, Table 3. However, the presence of D3 and

D4 bands denotes the amorphous and disordered carbon on the carbon deposits. The crystallite size of the carbon deposits formed on NiMo/Al₂O₃ was 38.5nm, which is 2.5 higher compared to NiMo/SBA-15. Probably, the deactivation was more pronounced since the sizes are much bigger than the pore sizes of alumina support, around 7.9nm.

Table 3
Properties of carbon deposits formed on the catalysts surface after the hydro deoxygenation of guaiacol.

Catalysts	Ratio I _D /I _G	Carbon crystallite size (nm)
NiMo/SBA-15	2,05	18,8
NiMo/Al ₂ O ₃	0,99	38,5

Thermogravimetric and Thermodifferential analyses

Thermogravimetric analyses of the spent catalysts were performed with air flow and increasing temperature at 10 °Cmin⁻¹ up to 900 °C. The TGA and DTA results are presented in Table 4, that shows water elimination of 11.1 % and physisorbed water [57, 58]. At higher temperature the weight loss was 1.8 % due to the decomposition of silanol and siloxane groups, which suggests high stability of the support at high temperatures [58, 59]. The spent NiMo/SBA-15 catalysts showed less water elimination (5.6 %). However, the exothermal peak at 305°C and the endothermic peaks at 431 and 536°C indicate coke burn. Then, comparing the mass loss of the fresh and spent catalysts, there is a loss of 3.1 %, and the carbon deposition rate was 1,14 mg_{coke}g_{cat}⁻¹ h⁻¹.

Table 4
Results of the weight loss for the spent and fresh catalysts from thermogravimetric curves.

Catalyst	Initial Weight (mg)	Temperature Range (°C)	Weight loss (%)	Coke formation ($\text{mg}_{\text{coke}} \text{g}_{\text{cat}}^{-1} \text{h}^{-1}$)
NiMo/SBA-15 fresh	2.5	25–300	11,1	-
		300–900	1,8	
NiMo/SBA-15spent (28 h)	2.5	25–250	5,6	1.14
		250–900	4,9	
NiMo/Al ₂ O ₃ fresh	11.2	25–150	9,3	-
		150–840	6,5	
		840–900	6,9	
NiMo/Al ₂ O ₃ spent (36 h)	11.2	25–250	2,4	1.65
		250–840	12,1	
		840–900	6,5	

The carbon deposition rate was $1.65 \text{ mg}_{\text{coke}} \text{g}_{\text{cat}}^{-1} \text{h}^{-1}$ for NiMo/Al₂O₃. In addition, the sublimation of MoO₃ occurred at 836°C, corresponding to a mass loss of 6.5 % as observed for the non-used sample. Comparing to Olcese's et al. work [60], the carbon deposition rate was $3.2 \text{ mg}_{\text{coke}} \text{g}_{\text{cat}}^{-1} \text{h}^{-1}$ after HDO reaction of guaiacol on 10 % Fe/SiO₂ catalyst.

TPO analyses

Temperature programmed oxidation was employed for catalysts before and after reaction, using a mixture of 5% O₂/He and exit gases were analyzed by mass spectroscopy, as shown in Fig. 7.

The results showed the mass signals of CO, CO₂ and H₂ before and after reaction. For the fresh NiMo/SBA-15 the profiles didn't show any important signal of CO or CO₂, indicating that all organic products present were eliminated during the calcination. But, the H₂ profile presented two broad peaks at 250 and 560 °C, which are attributed to elimination of hydroxyls groups present at the silica surface [61].

After reaction we observe three broad peaks from room temperature up to 600 °C, with maximum at 371 °C for H₂, at 400 °C for CO and at 276 °C for CO₂, which indicates decomposition of the coke formed at the surface during the HDO reaction.

Considering CO₂ as reference, due to the total combustion of carbon, we suggest that most coke deposited on the NiMo/SBA-15 are of polymeric types, such as carbon nanotubes, carbon nanofibers with

low weight, because the production of CO₂ occurred at low temperature (276°C). According to Lee et al. [62], this behavior could be assigned to the burning of light and well-organized carbonaceous species. However, the broad peak indicates also the presence of different carbon materials of polymerization products, as also observed by Kim et al. [63] for ethanol reforming on Ni/SBA-15 e NiMo/SBA-15 catalysts. In fact, nickel promoted the polymerization of ethylene, while molybdenum the partial oxidation, resulting in CO adsorption, which was deposited as coke around metallic particles, like small donuts circling the metallic active sites. In fact, Omoregbe et al. and Wang et al. [64, 65] proved that graphitic carbon on metallic sites burns at temperatures above 550 °C, while polymeric carbon burnt at lower temperatures. These authors observed the influence of the support with higher Lewis sites concentrations tend to improve the adsorption of acids, and carbon dioxide, which can reduce the carbon deposition.

On the other hand, the fresh NiMo/Al₂O₃ showed higher H₂ formation than the NiMo/SBA-15 sample, which are assigned to the higher hydroxyl content at the alumina surface [66]. The low CO and CO₂ formation at lower temperature are organic impurities adsorbed on the alumina support. However, the spent catalyst displayed high amounts of de H₂, CO e CO₂ formation, certainly due to the carbon deposition at the surface. For all signals it is possible to see two peaks, the first one at 50 °C extended to 250 °C and the second one from 250 to 600 °C, with maximum around 415 and 450 °C. These results suggest two different carbon species deposited, one less organized and with low weight for lower temperatures and the other one well-structured and higher weight burning at higher temperatures. The first coke burnt up to 250 °C are assigned to aromatic organic compounds with low polymerization degree and strongly adsorbed at the surface. These results reinforce the FTIR results indicating aromatic bonds of type C = C, C-H and C-O adsorbed on the surface of the materials, which agrees with Olcese et al. [60], for the HDO on a Fe/SiO₂ catalyst. Indeed, these carbons are quite different from those deposited on SBA-15 materials. The carbon deposits formed on NiMo/Al₂O₃ are predominantly graphite carbons. These carbons allotropes have well organized and dense structures when compared to the carbon nanotubes and nanofibers observed for the NiMo/SBA-15 catalyst [16, 55, 62].

Paivi et al [67] studied the Hydro deoxygenation (HDO) of bio-oils, lignin and the reaction catalyst stability with time-on-stream for understanding the industrial utilization of biomass in HDO to produce fuels and chemicals. Our results showed that more oxygenated feedstock, as well as presence of certain catalyst poisons influence the HDO performance and the results evidence carbon allotropes.

Conclusions

Comparing the selectivity of both catalysts, three main aspects may be analyzed: the selectivity of non-oxygenated compounds is higher on NiMo/SBA-15 than on NiMo/Al₂O₃; the selectivity to phenol is higher on NiMo/Al₂O₃ and the deoxygenated compounds (catechol, methyl guaiacol and derivatives). The SBA-15 support presents basically Si-OH groups, which act as Lewis acid sites and has higher ability for direct demethoxylation of guaiacol resulting in phenol.

After reaction it is noteworthy to observe significant modification in the IR spectrum of the silica catalyst. New bands appeared at 1390 and 1470 cm^{-1} , which are assigned to the rotation vibration and folding of C-H bonds of methyl groups. The formation of CH_3 groups at the catalysts surface during the reaction is closely related to the deactivation due to the carbon deposition on its surface. After reaction the spectrum of the alumina supported catalyst presented significant differences in the range 1000 and 1600 cm^{-1} , with appearance of new bands which are attributed to the unfolding C-H band bonded to the aromatic rings.

After reaction, the infrared spectroscopy showed that the alumina-supported catalyst contained deposits of aromatic and oxygenated organic substances, while the carbon deposited on SBA-15 materials are mainly the aliphatic type of simpler molecules. TPO analyses showed that the carbons deposited on the NiMo/SBA-15 catalyst were light polymer types, mainly nanotubes and nanofibers, while on the alumina catalyst it was of graphite type and heavier carbons were formed. This data was confirmed by Raman spectroscopy, displaying disorganized and defective carbonaceous structures on NiMo/SBA-15. On the other hand, in the alumina, the graphitic carbon was found in a greater proportion than in the previous one, besides structures of amorphous carbon and graphite defective. TGA analyses presented the amount of coke deposition after HDO, 1.14 and 1.65 $\text{mg}_{\text{coke}} \text{g}_{\text{cat}}^{-1} \text{h}^{-1}$ on SBA-15 and alumina, respectively.

List Of Abbreviations

DRIFTS: Diffuse Reflectance Infrared Transmission Spectroscopy

Raman: Raman spectroscopy

TPO: Temperature Programmed Oxidation

HDO: Hydrodeoxygenation

TPD: Temperature Programmed Desorption

FTIR: Fourier Transform Infrared spectroscopy

TGA and DTA: Thermogravimetric and Thermodifferential Analyses

Declarations

Ethics approval and consent to participate: Not applicable.

Consent to publication: Not applicable.

Availability of data and materials: The datasets used and/or analyzed during the current study are available from the corresponding author as requested.

Competing interests: The authors declare that they have no competing interests.

Funding: This work was supported by the Coordenação de Aperfeiçoamento de Pessoal de Nível Superior - Brasil (CAPES) - Finance Code 001 and by Conselho Nacional de Desenvolvimento Científico e Tecnológico CNPq 1

Authors' contributions: Rubens W.S. Lima performed the experiments and wrote the first draft of the manuscript under the constant technical guidance of Thiago L.R. Hwer. Rita M.B.Alves revised the manuscript and Martin Schmal, provided the research idea along with discussion and revision of the final text.

Acknowledgements: The authors would like to thank Dr. Rodrigo Bonfim from NUCAT-UFRJ for help with catalyst characterization. Thanks to University of S.Paulo, LAPCat and FAPESP for supporting the research program

References

1. Harrabin R (2012) UN climate talks extend Kyoto Protocol, promise compensation, BBC NEWS Sci. <https://www.bbc.com/news/science-environment-20653018> (accessed November 1, (2018))
2. Espinosa P, Mezouar S, Paris Agreement Enters into Force – Celebration and Reality Check, United Nation Clim. Chang. Opin (2016) <https://unfccc.int/index.php/news/paris-agreement-enters-into-force-celebration-and-reality-check> (accessed October 25, 2018)
3. Asadieraghi M, Wan Daud WMA, Abbas HF (2014) Model compound approach to design process and select catalysts for in-situ bio-oil upgrading. *Renew Sustain Energy Rev* 36:286–303. <https://doi.org/10.1016/j.rser.2014.04.050>
4. Bu Q, Lei H, Zacher AH, Wang L, Ren S, Liang J, Wei Y, Liu Y, Tang J, Zhang Q, Ruan R (2012) A review of catalytic hydrodeoxygenation of lignin-derived phenols from biomass pyrolysis. *Bioresour Technol* 124:470–477. <https://doi.org/10.1016/j.biortech.2012.08.089>
5. Saidi M, Samimi F, Karimipourfard D, Nimmanwudipong T, Gates BC, Rahimpour MR (2014) Upgrading of lignin-derived bio-oils by catalytic hydrodeoxygenation. *Energy Environ Sci* 7:103–129. <https://doi.org/10.1039/C3EE43081B>
6. Loricera CV, Pawelec B, Infantes-Molina A, Álvarez-Galván MC, Huirache-Acuña R, Nava R, Fierro JLG (2011) Hydrogenolysis of anisole over mesoporous sulfided CoMoW/SBA-15(16) catalysts, *Catal. Today* 172:103–110. <https://doi.org/10.1016/j.cattod.2011.02.037>
7. Sankaranarayanan TM, Berenguer A, Ochoa-Hernández C, Moreno I, Jana P, Coronado JM, Serrano DP, Pizarro P (2015) Hydrodeoxygenation of anisole as bio-oil model compound over supported Ni and Co catalysts: Effect of metal and support properties. *Catal Today* 243:163–172. <https://doi.org/10.1016/j.cattod.2014.09.004>
8. Zhao C, Lercher JA (2012) Selective Hydrodeoxygenation of Lignin-Derived Phenolic Monomers and Dimers to Cycloalkanes on Pd/C and HZSM-5 Catalysts, *ChemCatChem*. 4 64–68.

<https://doi.org/10.1002/cctc.201100273>

9. Ausavasukhi A, Huang Y, To AT, Sooknoi T, Resasco DE (2012) Hydrodeoxygenation of m-cresol over gallium-modified beta zeolite catalysts. *J Catal* 290:90–100.
<https://doi.org/10.1016/j.jcat.2012.03.003>
10. Hong D-Y, Miller SJ, Agrawal PK, Jones CW (2010) Hydrodeoxygenation and coupling of aqueous phenolics over bifunctional zeolite-supported metal catalysts. *Chem Commun* 46:1038–1040.
<https://doi.org/10.1039/B918209H>
11. Santos JL, Alda-Onggar M, Fedorov V, Peurla M, Eränen K, Mäki-Arvela P, Centeno M, Murzin DY (2018) Hydrodeoxygenation of vanillin over carbon supported metal catalysts. *Appl Catal A Gen* 561:137–149. <https://doi.org/10.1016/j.apcata.2018.05.010>
12. Dongil AB, Pastor-Pérez L, Sepúlveda-Escribano A, García R, Escalona N (2016) Hydrodeoxygenation of guaiacol: Tuning the selectivity to cyclohexene by introducing Ni nanoparticles inside carbon nanotubes. *Fuel* 172:65–69. <https://doi.org/10.1016/j.fuel.2016.01.002>
13. Centeno A, Laurent E, Delmon B (1995) Influence of the Support of CoMo Sulfide Catalysts and of the Addition of Potassium and Platinum on the Catalytic Performances for the Hydrodeoxygenation of Carbonyl, Carboxyl, and Guaiacol-Type Molecules. *J Catal* 154:288–298.
<https://doi.org/10.1006/jcat.1995.1170>
14. Furimsky E, Massoth FE (1999) Deactivation of hydroprocessing catalysts. *Catal Today* 52:381–495.
[https://doi.org/10.1016/S0920-5861\(99\)00096-6](https://doi.org/10.1016/S0920-5861(99)00096-6)
15. Cordero-Lanzac T, Palos R, Hita I, Arandes JM, Rodríguez-Mirasol J, Cordero T, Bilbao J, Castaño P (2018) Revealing the pathways of catalyst deactivation by coke during the hydrodeoxygenation of raw bio-oil. *Appl Catal B Environ* 239:513–524. <https://doi.org/10.1016/j.apcatb.2018.07.073>
16. Echeandia S, Pawelec B, Barrio VL, Arias PL, Cambra JF, Loricera CV, Fierro JLG (2014) Enhancement of phenol hydrodeoxygenation over Pd catalysts supported on mixed HY zeolite and Al₂O₃. An approach to O-removal from bio-oils. *Fuel* 117:1061–1073.
<https://doi.org/10.1016/j.fuel.2013.10.011>
17. Hwer TLR, Souza AGF, Roseno KTC, Moreira PF, Bonfim R, Alves RMB, Schmal M (2018) Influence of acid sites on the hydrodeoxygenation of anisole with metal supported on SBA-15 and SAPO-11. *Renew Energy* 119:615–624. <https://doi.org/10.1016/j.renene.2017.12.044>
18. Matos JR, Mercuri LP, Kruk M, Jaroniec M (2001) Toward the synthesis of extra-large-pore MCM-41 analogues. *Chem Mater* 13:1726–1731. <https://doi.org/10.1021/cm000964p>
19. Brunauer S, Emmett PH, Teller E (1938) Adsorption of Gases in Multimolecular Layers. *J Am Chem Soc* 60:309–319. <https://doi.org/10.1021/ja01269a023>
20. Barrett EP, Joyner LG, Halenda PP (1951) The Determination of Pore Volume and Area Distributions in Porous Substances. I. Computations from Nitrogen Isotherms. *J Am Chem Soc* 73:373–380.
<https://doi.org/10.1021/ja01145a126>
21. Pimenta MA, Dresselhaus G, Dresselhaus MS, Cançado LG, Jorio A, Saito R (2007) Studying disorder in graphite-based systems by Raman spectroscopy, *Phys Chem Chem Phys* 9:1276–1290.

<https://doi.org/10.1039/B613962K>

22. Hellinger M, Carvalho HWP, Baier S, Wang D, Kleist W, Grunwaldt JD (2015) Catalytic hydrodeoxygenation of guaiacol over platinum supported on metal oxides and zeolites. *Appl Catal A Gen* 490:181–192. <https://doi.org/10.1016/j.apcata.2014.10.043>
23. Popov A, Kondratieva E, Goupil JM, Mariey L, Bazin P, Gilson J-P, Travert A, Maugé F (2010) Bio-oils Hydrodeoxygenation: Adsorption of Phenolic Molecules on Oxidic Catalyst Supports. *J Phys Chem C* 114:15661–15670. <https://doi.org/10.1021/jp101949j>
24. Rochester CH, Trebilco D-A (1978) Infrared study of the adsorption of phenols on silica immersed in heptane. *J Chem Soc Faraday Trans 1 Phys Chem Condens Phases* 74:1137. <https://doi.org/10.1039/f19787401137>
25. Rochester CH, Trebilco D-A (1978) Infrared study of the adsorption of anisoles on silica immersed in heptane. *J Chem Soc Faraday Trans 1 Phys Chem Condens Phases* 74:1125. <https://doi.org/10.1039/f19787401125>
26. Gutierrez A, Kaila RK, Honkela ML, Slioor R, Krause AOI (2009) Hydrodeoxygenation of guaiacol on noble metal catalysts. *Catal Today* 147:239–246. <https://doi.org/10.1016/j.cattod.2008.10.037>
27. Leiva K, Martinez N, Sepulveda C, García R, Jiménez CA, Laurenti D, Vrinat M, Geantet C, Fierro JLG, Ghampson IT, Escalona N (2015) Hydrodeoxygenation of 2-methoxyphenol over different Re active phases supported on SiO₂ catalysts. *Appl Catal A Gen* 490:71–79. <https://doi.org/10.1016/j.apcata.2014.10.054>
28. Olcese RN, Bettahar M, Petitjean D, Malaman B, Giovanella F, Dufour A (2012) Gas-phase hydrodeoxygenation of guaiacol over Fe/SiO₂ catalyst. *Appl Catal B Environ* 115–116:63–73. <https://doi.org/10.1016/j.apcatb.2011.12.005>
29. Bui VN, Laurenti D, Afanasiev P, Geantet C (2011) Hydrodeoxygenation of guaiacol with CoMo catalysts. Part I: Promoting effect of cobalt on HDO selectivity and activity. *Appl Catal B Environ* 101:239–245. <https://doi.org/10.1016/j.apcatb.2010.10.025>
30. Ghampson IT, Sepúlveda C, Garcia R, Frederick BG, Wheeler MC, Escalona N, Desisto WJ (2012) Guaiacol transformation over unsupported molybdenum-based nitride catalysts. *Appl Catal A Gen* 413–414:78–84. <https://doi.org/10.1016/j.apcata.2011.10.050>
31. Sepúlveda C, Leiva K, García R, Radovic LR, Ghampson IT, DeSisto WJ, Fierro JLG, Escalona N (2011) Hydrodeoxygenation of 2-methoxyphenol over Mo₂N catalysts supported on activated carbons. *Catal Today* 172:232–239. <https://doi.org/10.1016/j.cattod.2011.02.061>
32. Yang Y, Ochoa-Hernández C, de la Peña VA, O’Shea P, Pizarro JM, Coronado DP, Serrano (2014) Effect of metal–support interaction on the selective hydrodeoxygenation of anisole to aromatics over Ni-based catalysts. *Appl Catal B Environ* 145:91–100. <https://doi.org/10.1016/j.apcatb.2013.03.038>
33. Robinson AM, Hensley JE, Medlin JW (2016) Bifunctional Catalysts for Upgrading of Biomass-Derived Oxygenates: A Review. *ACS Catal* 6:5026–5043. <https://doi.org/10.1021/acscatal.6b00923>
34. Bui VN, Laurenti D, Afanasiev P, Geantet C (2011) Hydrodeoxygenation of guaiacol with CoMo catalysts. Part I: Promoting effect of cobalt on HDO selectivity and activity. *Appl Catal B Environ*

- 101:239–245. <https://doi.org/10.1016/j.apcatb.2010.10.025>
35. Bui VN, Laurenti D, Delichère P, Geantet C (2011) Hydrodeoxygenation of guaiacol Part II: Support effect for CoMoS catalysts on HDO activity and selectivity. *Appl Catal B Environ* 101:246–255. <https://doi.org/10.1016/j.apcatb.2010.10.0311>
36. Azimov F, Markova I, Stefanova V, Sharipov K (2012) Synthesis and Characterization of SBA-15 and Ti-SBA-15 Nanoporous Materials for DME Catalysts. *Sharipov J Univ Chem Technol Metall* 47:333–340
37. Pudukudy M, Yaakob Z, Akmal ZS (2015) Direct decomposition of methane over Pd promoted Ni/SBA-15 catalysts. *Appl Surf Sci* 353:127–136. <https://doi.org/10.1016/j.apsusc.2015.06.073>
38. Shao X, Zhang X, Yu W, Wu Y, Qin Y, Sun Z, Song L (2012) Effects of surface acidities of MCM-41 modified with MoO₃ on adsorptive desulfurization of gasoline. *Appl Surf Sci* 263:1–7. <https://doi.org/10.1016/j.apsusc.2012.07.142>
39. Sohn JR, Chun EW, Il Paet Y (2003) Spectroscopic Studies on ZrO₂ Modified with MoO₃ and Activity for Acid Catalysis. *Bull Korean Chem Soc* 24:1785–1792. <https://doi.org/10.5012/bkcs.2003.24.12.1785>
40. Hojabri A, Hajakbari F, Meibodi AE (2015) Structural and optical properties of nanocrystalline α -MoO₃ thin films prepared at different annealing temperatures. *J Theor Appl Phys* 9:67–73. <https://doi.org/10.1007/s40094-014-0161-5>
41. de Moura AP, de Oliveira LH, Rosa ILV, Xavier CS, Lisboa-Filho PN, Li MS, La Porta FA, Longo E, Varela JA (2015) Structural, Optical, and Magnetic Properties of NiMoO₄ Nanorods Prepared by Microwave Sintering. *Sci. World J* 20151–20158. <https://doi.org/10.1155/2015/315084>
42. Robert DLB, Silverstein M, Francis X, Webster DJ, Kiemle, *Spectrometric Identification of Organic Compounds*, 8th Edition, Wiley, Hoboken (2014) [https://doi.org/10.1016/0022-2860\(76\)87024-X](https://doi.org/10.1016/0022-2860(76)87024-X)
43. Popov A, Kondratieva E, Goupil JM, Mariey L, Bazin P, Gilson J-P, Travert A, Maugé F (2010) Bio-oils Hydrodeoxygenation: Adsorption of Phenolic Molecules on Oxidic Catalyst Supports. *J Phys Chem C* 114:15661–15670. <https://doi.org/10.1021/jp101949j>
44. Ghampson IT, Sepúlveda C, Garcia R, Frederick BG, Wheeler MC, Escalona N, Desisto WJ (2012) Guaiacol transformation over unsupported molybdenum-based nitride catalysts. *Appl Catal A Gen* 413–414:78–84. <https://doi.org/10.1016/j.apcata.2011.10.050>
45. Becerra M-E, Arias N-P, Giraldo O-H, López-Suárez F-E, Illán-Gómez M-J, Bueno-López A (2012) Alumina-Supported Manganese Catalysts for Soot Combustion Prepared by Thermal Decomposition of KMnO₄. *Catalysts*. 2: 352–367. <https://doi.org/10.3390/catal2030352>
46. Hosseini SA, Niaei A, Salari D (2011) Production of γ -Al₂O₃ from Kaolin. *Open J Phys Chem* 01:23–27. <https://doi.org/10.4236/ojpc.2011.12004>
47. Salahudeen N, Ahmed AS, Al-Muhtaseb AH, Dauda M, Waziri SM, Jibril BY (2015) Synthesis of gamma alumina from Kankara kaolin using a novel technique. *Appl Clay Sci* 105–106:170–177. <https://doi.org/10.1016/j.clay.2014.11.041>

48. Kassem M (2006) Phase relations in the Al₂O₃-MoO₃ and Al-MoO₃ systems, investigated by X-ray powder diffraction, FTIR, and DTA techniques, *Inorg Mater.* 42:165–42:170. <https://doi.org/10.1134/S0020168506020105>
49. Ayala-G M, Puello E, Quintana PP, González-García G, Diaz C (2015) Comparison between alumina supported catalytic precursors and their application in thiophene hydrodesulfurization: (NH₄)₄[NiMo₆O₂₄H₆]·5H₂O/γ-Al₂O₃ and NiMoO_x/γ-Al₂O₃ conventional systems. *RSC Adv* 5:102652–102662. <https://doi.org/10.1039/C5RA17695F>
50. Tyrone Ghampson I, Sepúlveda C, Garcia R, García Fierro JL, Escalona N, DeSisto WJ (2012) Comparison of alumina- and SBA-15-supported molybdenum nitride catalysts for hydrodeoxygenation of guaiacol, Guaiacol. *Appl Catal A Gen* 435–436:51–60. <https://doi.org/10.1016/j.apcata.2012.05.039>
51. Arun N, Maley J, Chen N, Sammynaiken R, Hu Y, Dalai AK (2017) NiMo nitride supported on γ-Al₂O₃ for hydrodeoxygenation of oleic acid: Novel characterization and activity study. *Catal Today* 291:153–159. <https://doi.org/10.1016/j.cattod.2017.03.053>
52. Kim D, Kwak BS, Park N-K, Han GB, Kang M (2015) Dynamic hydrogen production from ethanol steam-reforming reaction on Ni_xMo_y/SBA-15 catalytic system. *Int J Energy Res* 39:279–292. <https://doi.org/10.1002/er.3241>
53. Kong L, Li J, Zhao Z, Liu Q, Sun Q, Liu J, Wei Y (2016) Oxidative dehydrogenation of ethane to ethylene over Mo-incorporated mesoporous SBA-16 catalysts: The effect of MoO_x dispersion. *Appl Catal A Gen* 510:84–97. <https://doi.org/10.1016/j.apcata.2015.11.016>
54. Martins AR, Cunha IT, Oliveira AAS, Moura FCC (2017) Highly ordered spherical SBA-15 catalysts for the removal of contaminants from the oil industry. *Chem Eng J* 318:189–196. <https://doi.org/https://doi.org/10.1016/j.cej.2016.06.053>
55. Shanmugam V, Zapf R, Neuberg S, Hessel V, Kolb G (2017) Effect of ceria and zirconia promoters on Ni/SBA-15 catalysts for coking and sintering resistant steam reforming of propylene glycol in microreactors. *Appl Catal B Environ* 203:859–869. <https://doi.org/10.1016/j.apcatb.2016.10.075>
56. Kouketsu Y, Mizukami T, Mori H, Endo S, Aoya M, Hara H, Nakamura D, Wallis S (2014) A new approach to develop the Raman carbonaceous material geothermometer for low-grade metamorphism using peak width. *Isl Arc* 23:33–50. <https://doi.org/10.1111/iar.12057>
57. Gouveia Gil A, Wu Z, Chadwick D, Li K, Ni/SBA-15 (2015) Catalysts for combined steam methane reforming and water gas shift—Prepared for use in catalytic membrane reactors. *Appl Catal A Gen* 506:188–196. <https://doi.org/10.1016/j.apcata.2015.09.009>
58. Paul L, Banerjee B, Bhaumik A, Ali M (2016) Functionalized SBA-15 supported nickel (II)–oxime–imine catalysts for liquid phase oxidation of olefins under solvent-free conditions. *J Solid State Chem* 237:105–112. <https://doi.org/10.1016/j.jssc.2016.01.018>
59. Occelli M, Biz S, Auroux A (1999) Effects of isomorphous substitution of Si with Ti and Zr in mesoporous silicates with the MCM-41 structure. *Appl Catal A Gen* 183:231–239. [https://doi.org/10.1016/S0926-860X\(99\)00059-9](https://doi.org/10.1016/S0926-860X(99)00059-9)

60. Olcese R, Bettahar MM, Malaman B, Ghanbaja J, Tibavizco L, Petitjean D, Dufour A (2013) Gas-phase hydrodeoxygenation of guaiacol over iron-based catalysts. Effect of gases composition, iron load and supports (silica and activated carbon). *Appl Catal B Environ* 129:528–538.
<https://doi.org/10.1016/j.apcatb.2012.09.043>
61. Luan Z, Fournier JA, Wooten JB, Miser DE, Chang MJ (2005) Functionalized mesoporous SBA-15 silica molecular sieves with mercaptopropyl groups: Preparation, characterization and application as adsorbents, *Stud Surf Sci Catal*, 897–906. [https://doi.org/10.1016/S0167-2991\(05\)80302-7](https://doi.org/10.1016/S0167-2991(05)80302-7)
62. Lee J-H, Lee E-G, Joo O-S, Jung K-D (2004) Stabilization of Ni/Al₂O₃ catalyst by Cu addition for CO₂ reforming of methane. *Appl Catal A Gen* 269:1–6. <https://doi.org/10.1016/j.apcata.2004.01.035>
63. Kim B, Kim Y, Jae J, Watanabe C, Kim S, Jung S, Chai S, Park Y (2015) Bioresource Technology Pyrolysis and catalytic upgrading of Citrus unshiu peel. *Bioresour Technol* 194:312–319.
<https://doi.org/10.1016/j.biortech.2015.07.035>
64. Omoregbe O, Danh HT, Abidin SZ, Setiabudi HD, Abdullah B, Vu KB, Vo D-VN (2016) Influence of Lanthanide Promoters on Ni/SBA-15 Catalysts for Syngas Production by Methane Dry Reforming. *Procedia Eng* 148:1388–1395. <https://doi.org/10.1016/j.proeng.2016.06.556>
65. Wu X, Jiang P, Jin F, Liu J, Zhang Y, Zhu L, Xia T, Shao K, Wang T, Li Q (2017) Production of jet fuel range biofuels by catalytic transformation of triglycerides based oils. *Fuel* 188:205–211.
<https://doi.org/10.1016/j.fuel.2016.10.030>
66. Costa TMH, Gallas MR, Benvenuto EV, da Jornada JAH (1999) Study of Nanocrystalline γ -Al₂O₃ Produced by High-Pressure Compaction. *J Phys Chem B* 103:4278–4284.
<https://doi.org/10.1021/jp983791o>
67. Päivi Mäki-Arvela and Dmitry Yu. Murzin (2017) Hydrodeoxygenation of Lignin-Derived Phenols: From Fundamental Studies towards Industrial Applications, *Catalysts*, 7: 9 265;
<https://doi.org/10.3390/catal7090265>

Figures

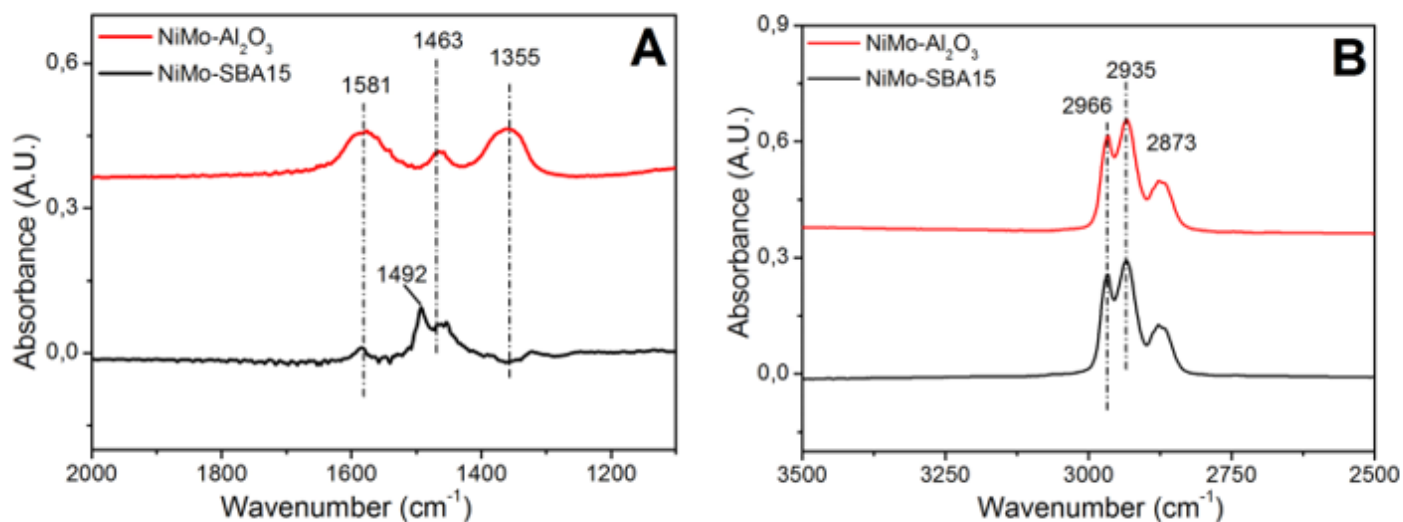


Figure 1

IR spectra of adsorbed guaiacol on NiMo-Al₂O₃ and NiMo-SBA15 catalysts at 200 °C.

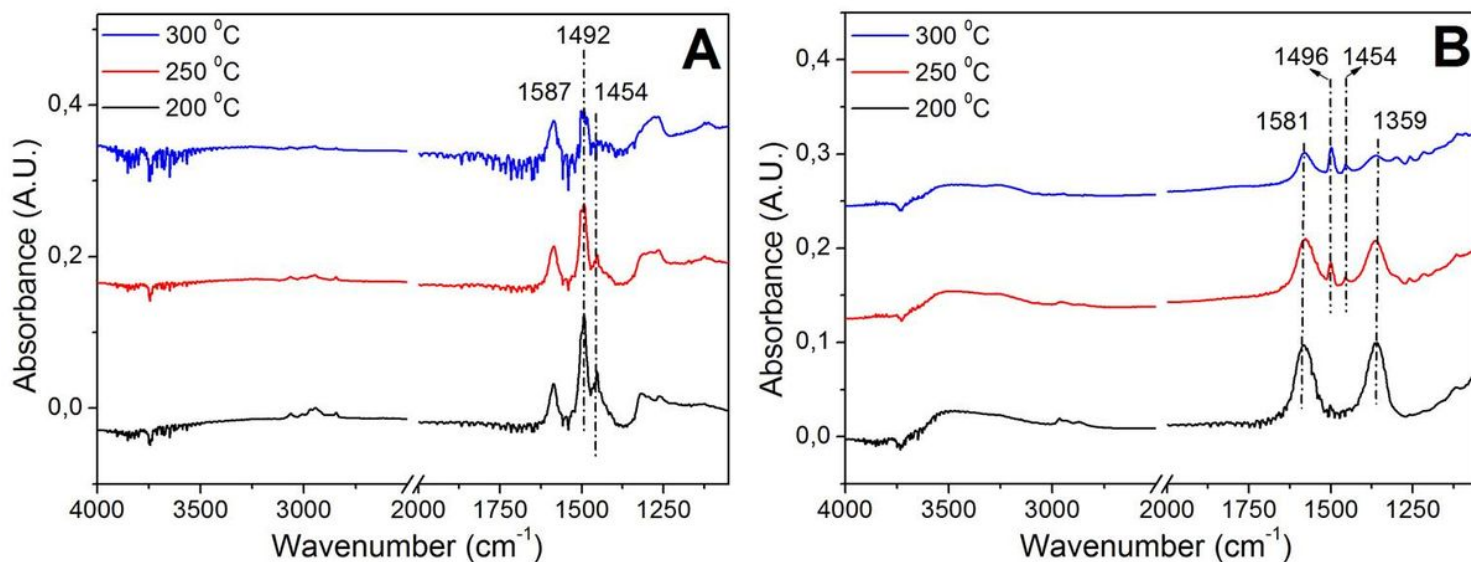


Figure 2

IR spectra of Guaiacol on NiMo-SBA15 (A) and NiMo-Al₂O₃ (B) catalysts after chamber evacuation at 200, 250 and 300 °C.

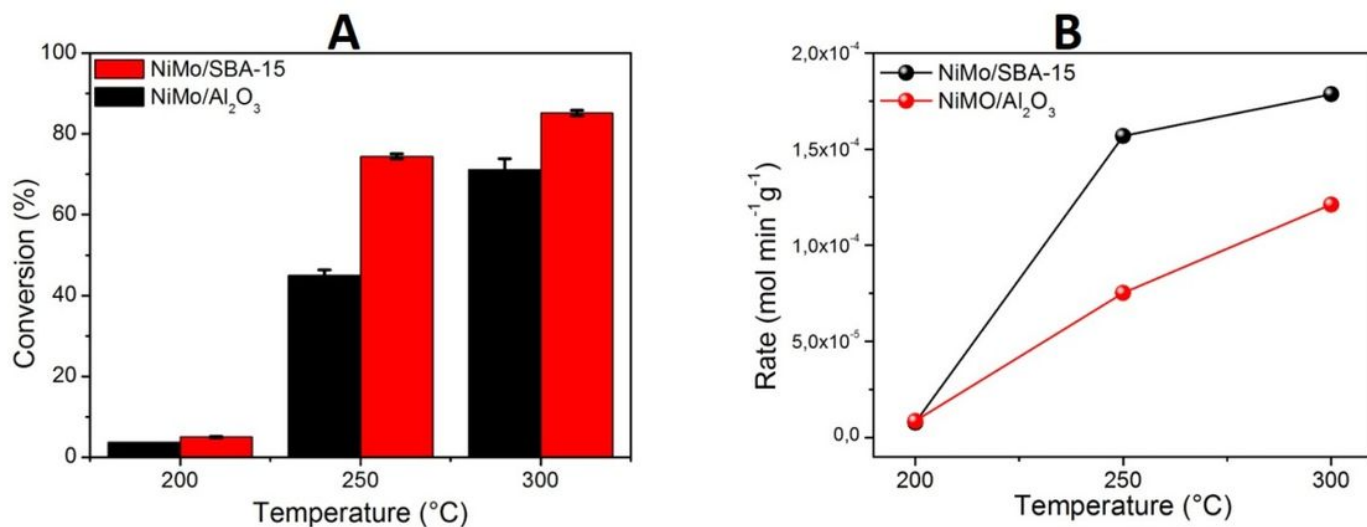


Figure 3

The support effect on the hydro deoxygenation of Guaiacol. A: Guaiacol conversion; B: Rate of the guaiacol hydro deoxygenation.

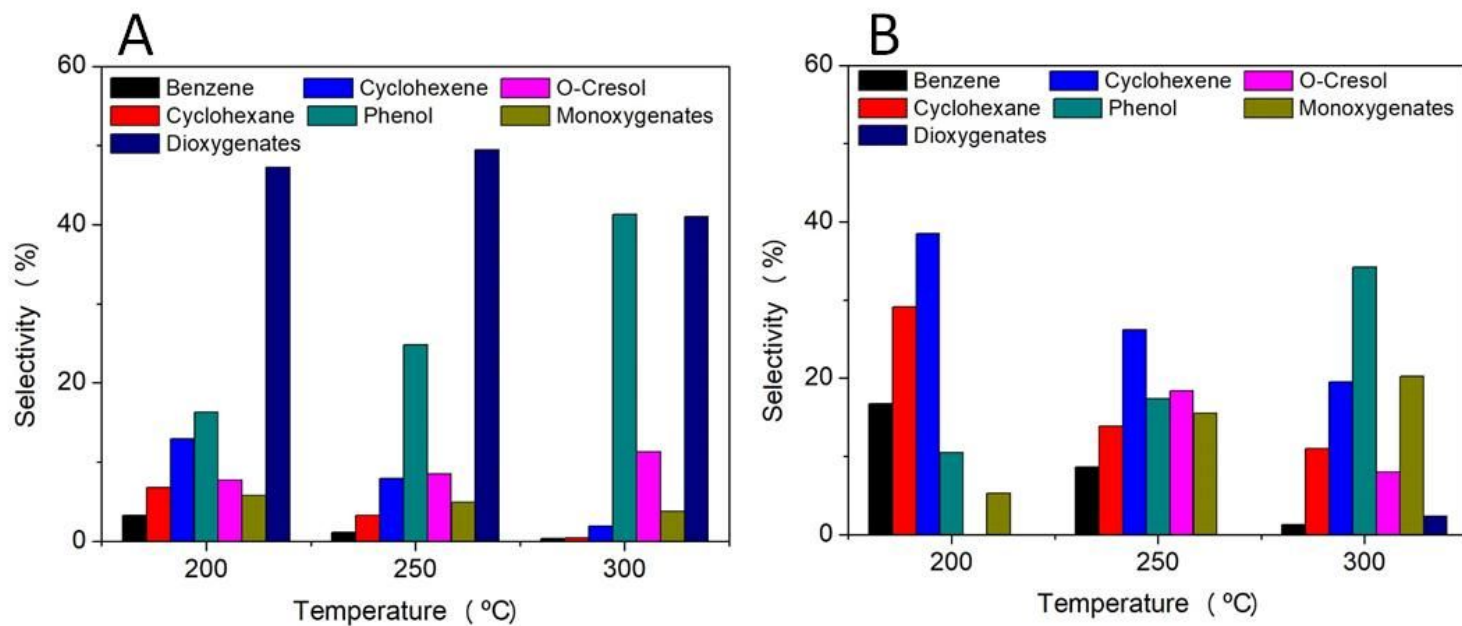


Figure 4

Selectivity and Product distribution on different catalysts

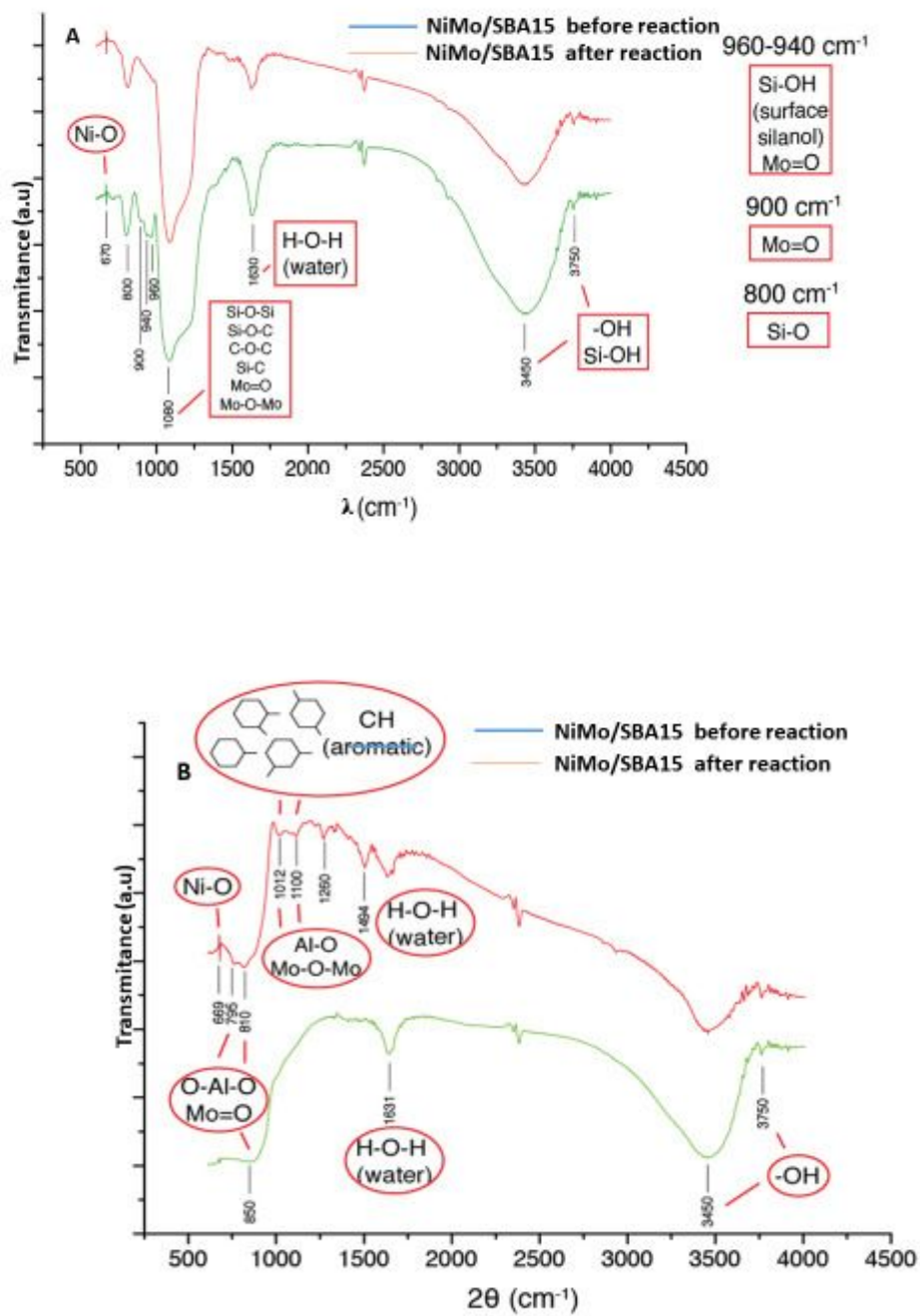


Figure 5

Infrared spectroscopy of the fresh and spent catalysts after Guaiacol hydrodeoxygenation. A: NiMo/SBA-15; B: NiMo/Al₂O₃.

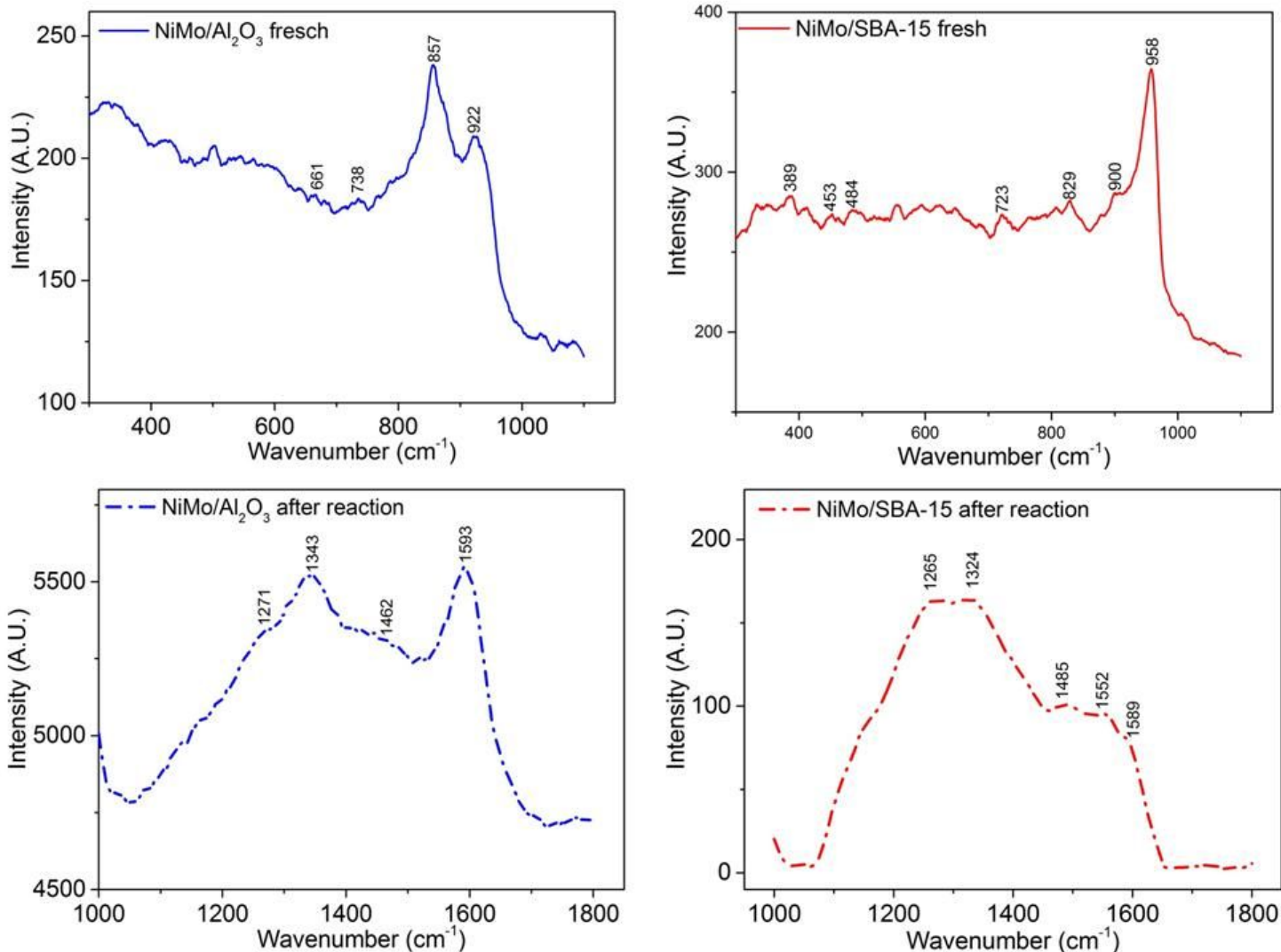


Figure 6

Raman spectrum of the catalysts NiMo/Al₂O₃ and NiMo/SBA-15 before and after hydro deoxygenation of guaiacol.

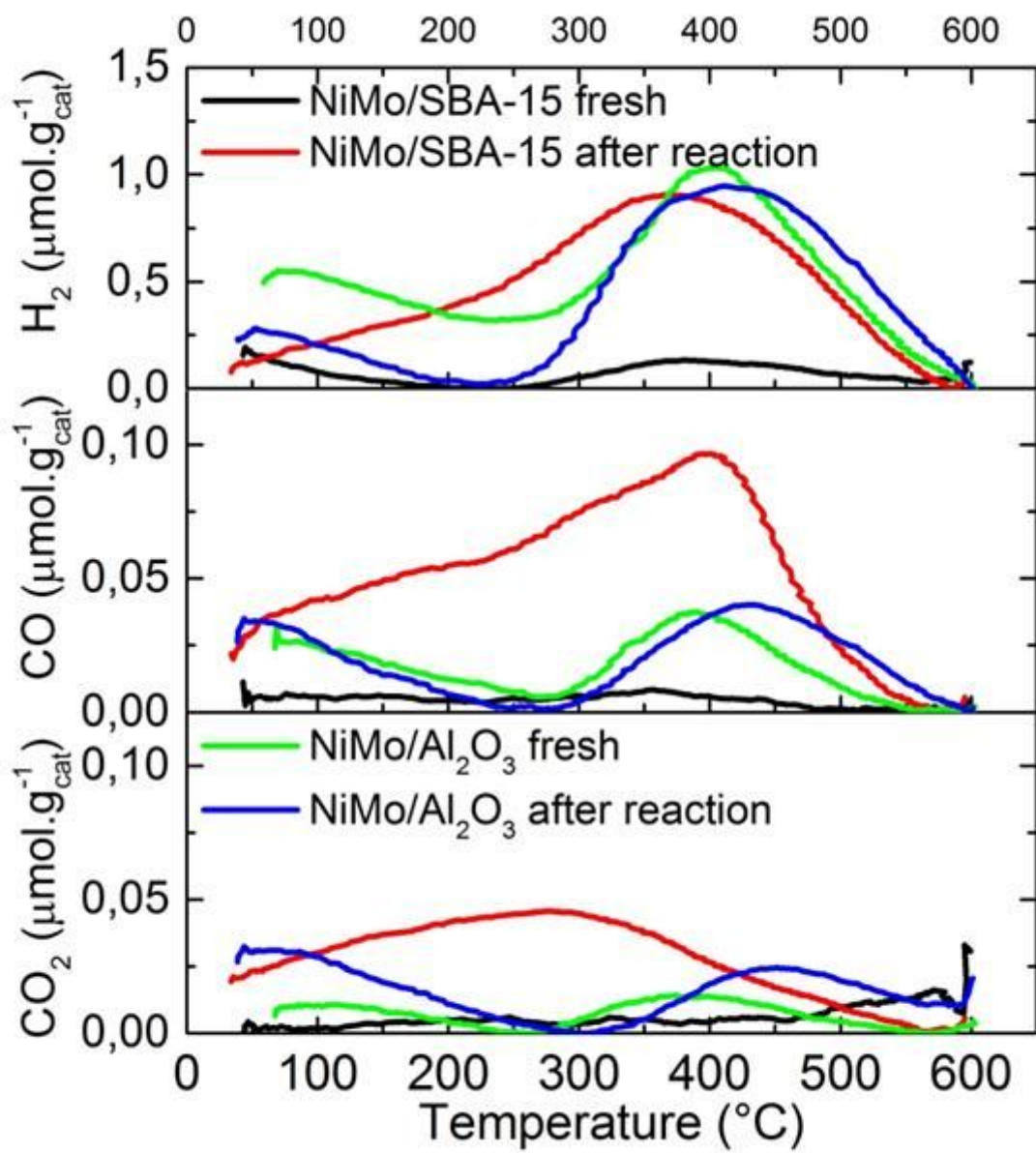


Figure 7

The Thermal programmed oxidation (TPO) analysis of catalysts until and after hydrodeoxygenation of guaiacol.

Supplementary Files

This is a list of supplementary files associated with this preprint. Click to download.

- [graphicalabstract1.pptx.docx](#)